Parameter Estimation for OJ 287

UCD School of Mathematics and Statistics Summer Internship

Adam Keyes & Brian Sheridan

August 1, 2022

Abstract

The OJ 287 system is a celestial object which exhibits quasi-periodic variations in its historically observed light curve. Previous attempts to model the system have achieved the best success using a supermassive binary black hole, or SMBBH model. The physical parameters of this system have previously been investigated, however there still exist opportunities to explore different methods of estimating these parameters and their uncertainties. In this project, we approach this problem using methods of Bayesian inference. This is achieved by first modelling the secondary black hole's trajectory with Kerr geodesic equations. Then, the accretion disk is modelled using the Shakura-Sunyaev/α disk model, however with the disk parameter α being a stochastically varying quantity, meaning that that the times of the observed flares in the light curve are random and taken to follow log-normal distributions. Finally, a parameter estimation algorithm is devised to estimate parameter values and uncertainties, through a combination of posterior optimisation and sampling. These parameter estimates allow us to compare the results of our model to previously observed optical outbursts of the system and also to make predictions for when the next flares in the light curve will be observed.

1 Introduction

Astronomical observations of the OJ 287 system exist for over a hundred years, having been captured on photographic plates as far back as 1887 [1]. The light curve of this celestial object, which graphs the light intensity over time, exhibits quasi-periodic variations over a period of about 12 years and also a longer period of about 60 years, as seen in Figure 1. Each outburst flare, or spike in intensity, exhibits a double-peaking behaviour, consisting of two peaks narrowly separated only by a year or two. The light from the system is redshifted by a factor of $z = 0.306$ [2], placing an estimate on the distance to the system at about 3.5 billion light years away from Earth. This also means that the observed period of the light variations in the Earth frame of about 12 years translates to about 9 years in the rest frame of the system.

The quasi-periodic, double peaked structure of the OJ 287 light curve inspired Sillanpää et al. in

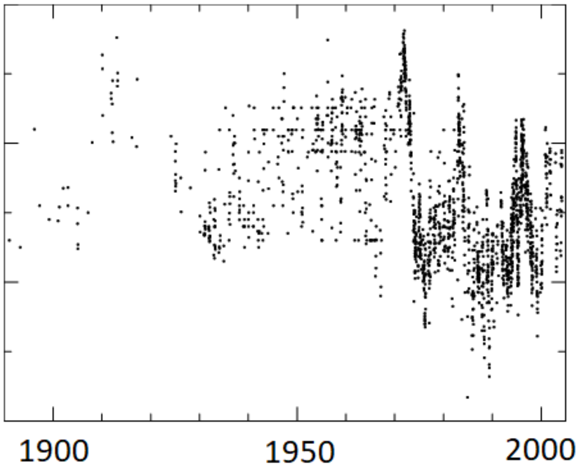

Figure 1: The historical light curve of OJ 287. Each point is a three day average [3].

1988 [4] to model the system as a supermassive black hole binary pair. This approach differed from previous models including those of a precessing relativistic jet or even a precessing accretion disk [5], which inaccurately predicted flare outburst times and failed to match the historical light curve. In the supermassive binary black hole model proposed by Sillanpää et al., an accretion disk surrounds a rotating supermassive primary black hole while a much less massive secondary black orbits the primary. When the secondary impacts the accretion disk, particles in the accretion disk are tidally perturbed from their orbits and thrown into the primary black hole which results in a flare. In this model, the 12 year quasi-period corresponds to the orbital period while the longer 60 year quasi-period corresponds to half of the full precession of the orbit around the orbital plane. This 60 year period corresponds to the semi-major axis of the orbit precessing from being, for example, perpendicular to the accretion disk through being parallel and then returning to being perpendicular to the accretion disk, this time however oriented in a direction directly opposite to its original orientation. Therefore the full precessional period would be estimated to be 120 years. The secondary also impacts the accretion disk twice per orbit, and due to the high eccentricity, this corresponds to the observed double peaked outbursts as the orbit comes close to the primary black hole.

Observed Outbursts
1912.98
1947.28
1957.01
1972.94
1982.96
1984.13
1995.84
2005.75
2007.69
2015.88
2019.57

Table 1: The outburst times of 11 well recorded observations of the OJ 287 system in Julian years. It is worth noting that the 2019 outburst was not directly observed, however its existence was inferred using the observed light curve from the 2015 outburst [1][6].

This model was further developed by Valtonen, with modern modelling from Dey, Valtonen and others [7] with outburst predictions which accurately matched the historical light curve [6], giving good support to the supermassive binary black hole model proposed by Sillanpää et al. The process of the flare emissions is however now different. When the secondary impacts the accretion disk, rather than particles being thrown into the primary black hole and causing a flare, plasma bubbles are formed which expand, cool and become optically thin. Once optically thin, the radiation inside the bubble escapes and is seen as a flare. An illustration of this process is shown in Figure 2. The general outline of the current model by Dey et al. is as follows.

Firstly, the equations of motion used to model the trajectory of the secondary black hole are post-Newtonian (PN) expansions, which aim to add higher order general relativistic corrections to Keplerian orbits stemming from Newtonian gravity [8]. Then, in their model for the time difference between impacts of the secondary with the accretion disk and associated outbursts, a *time delay* factor and a *time advance* factor are introduced. The former is attributed to the aforementioned formation and expansion of plasma bubbles, while the latter attributed to the bending of the accretion disk due to gravitational effects from the secondary black hole. The parameters are then estimated by varying them from some initial values and the equations of motion integrated such that a calculated outburst lies within a certain range of an observed outburst. This process is repeated until all calculated outbursts lie within a certain range of the observed ones and the resulting parameters are taken to be an “acceptable solution”.

Our goal in this report is to take a different approach to modelling the OJ 287 system, allowing us to use statistical techniques for the parameter estimation procedure. This is achieved in three main sections. Firstly, the equations of motion of the orbit of the secondary black hole around the primary are described, then a model for the accretion disk along with time delays between impacts and outbursts is made and finally a parameter estimation algorithm is designed, in order to give estimates along with uncertainties for the parameters of the OJ 287 system by comparing predictions with observed data from Table 1.

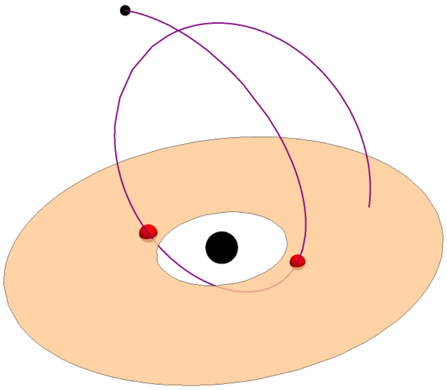

(a) Generic view of the orbit.

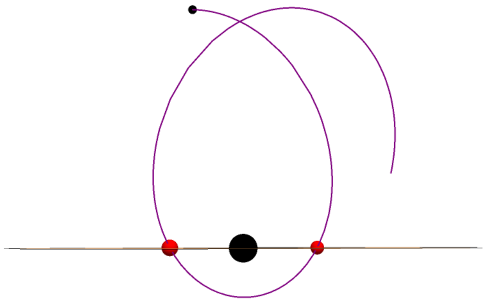

(b) Side view of the orbit.

Figure 2: Views of the orbital model for the OJ 287 system. Plasma bubbles are created on impact with the accretion disk, then expand and become optically thin to cause a flare. Illustrations not to scale.

2 Orbital Trajectory

2.1 Kerr Geodesics

The orbit of the secondary is assumed highly eccentric, leading its trajectory into the strong gravitational field of the primary black hole. This suggests that equations of motion suited to strong fields could be used instead of post-

Newtonian expansions. Along with this point, the assumed large mass ratio between the two black holes in the context of this problem motivates the use of Kerr geodesics to model the trajectory of the secondary. These equations describe the path of a test particle around a rotating black hole, thus providing a general mathematical framework for the possible trajectory of the secondary with which to work with (note that the accretion disk is assumed not to affect the trajectory of the secondary).

The Kerr geodesic equations of motion, in geometrised units where $G = c = 1$, are given as [9]

$$\begin{aligned}\left(\frac{dr}{d\lambda}\right)^2 &= (\mathcal{E}\bar{\omega}^2 - a\mathcal{L}_z)^2 \\ &\quad - \Delta(\mu^2 r^2 + (\mathcal{L}_z - a\mathcal{E})^2 + \mathcal{Q}) \\ &\equiv V_r(r; \mathcal{E}, \mathcal{L}_z, \mathcal{Q})\,, \end{aligned} \tag{1}$$

$$\begin{aligned}\left(\frac{d\theta}{d\lambda}\right)^2 &= \mathcal{Q} - \mathcal{L}_z^2 \cot^2\theta - a^2(\mu^2 - \mathcal{E}^2)\cos^2\theta \\ &\equiv V_\theta(\theta; \mathcal{E}, \mathcal{L}_z, \mathcal{Q})\,, \end{aligned} \tag{2}$$

$$\begin{aligned}\frac{dt}{d\lambda} &= \mathcal{E}\left(\frac{\bar{\omega}^4}{\Delta} - a^2\sin^2\theta\right) + a\mathcal{L}_z\left(1 - \frac{\bar{\omega}^2}{\Delta}\right) \\ &\equiv V_t(r, \theta; \mathcal{E}, \mathcal{L}_z, \mathcal{Q})\,, \end{aligned} \tag{3}$$

$$\begin{aligned}\frac{d\phi}{d\lambda} &= \mathcal{L}_z \csc^2\theta + a\mathcal{E}\left(\frac{\bar{\omega}^2}{\Delta} - 1\right) - \frac{a^2\mathcal{L}_z}{\Delta} \\ &\equiv V_\phi(r, \theta; \mathcal{E}, \mathcal{L}_z, \mathcal{Q})\,, \end{aligned} \tag{4}$$

where $\bar{\omega}^2 = r^2 + a^2$, $\Sigma = r^2 + a^2\cos^2\theta$ and $\Delta = r^2 - 2Mr + a^2$, although we can take the total mass $M = 1$ to simplify calculations.

The equations are parameterised with respect to *Mino time* λ, defined through

$$\frac{d\tau}{d\lambda} = \Sigma\,, \tag{5}$$

with τ denoting proper time. The advantage of parameterising the equations of motion with Mino time is that the equations for the radial coordinate, r, and the polar angle coordinate, θ, become decoupled. This means that each of these two equations, V_r and V_θ, is only a function of the respective coordinate itself, along with the three constants of motion, the energy $\mathcal{E}$, the axial angular momentum $\mathcal{L}_z$ and Carter's constant $\mathcal{Q}$. This makes finding solutions to the equations of motion more tractable.

A convenient parameterisation for the orbital constants of motion uses $(p, e, \theta_{\min})$, where p denotes the semi-latus rectum of the orbit, e the eccentricity and $\theta_{\min}$ the minimum polar angle of the Kerr geodesic orbits. This parameterisation is the approach used in this investigation. The relationship between these and the constants $(\mathcal{E}, \mathcal{L}_z, \mathcal{Q})$ was first derived by Schmidt [10] and is outlined in Appendix A. This allows the Kerr geodesic equations to then be parameterised with the more convenient $(p, e, \theta_{\min})$.

The given equations of motion could be solved numerically, however the separability given by using Mino time allows analytic solutions for bound Kerr geodesic equations to be found, originally derived by Fujita and Hikida [11]. These solutions are organised into a compact form by Van de Meent [12] and are used here to analytically calculate the orbits.

The analytical expressions characterising the Kerr geodesics make heavy use of Jacobi elliptic functions and integrals. This is, however, advantageous since these functions and integrals can be computed very quickly using computational tools such as MATHEMATICA, where, for example, an elliptic integral can be calculated on the order of about $O(10^{-6})$ seconds. This means that calculation of candidate orbits can be executed very quickly in the parameter estimation algorithm which will allow more trials to be performed.

The analytical expression from Van de Meent governing the radial coordinate is given as

$$r(q_r) = \frac{r_3(r_1 - r_2)\mathrm{sn}^2(\frac{K(k_r)}{\pi}q_r|k_r) - r_2(r_1 - r_3)}{(r_1 - r_2)\mathrm{sn}^2(\frac{K(k_r)}{\pi}q_r|k_r) - (r_1 - r_3)}\,, \tag{6}$$

where sn is the Jacobi elliptic sine function, K the complete elliptic integral of the first kind and q_r is the phasing of the radial coordinate, which is a function of Mino time, λ, and is given as

$$q_r(\lambda) = \Upsilon_r\lambda + q_{r,0}\,, \tag{7}$$

with Υ_r the radial frequency in Mino time and $q_{r,0}$ the initial radial phase of the orbital trajectory. This initial phase is a parameter which is optimised for in the parameter estimation algorithm, since we do not know beforehand what the initial phase of the orbit is at the time of the first impact.

The form of the solution for the coordinate time t is given as

$$t(q_t, q_r, q_z) = q_t + t_r(q_r) + t_z(q_z)\,. \tag{8}$$

We see that it is a function of the three phases, q_t, q_r and q_z, which are all in turn functions of Mino time λ and of similar mathematical form to Equation (7), such that

$$q_t(\lambda) = \Upsilon_t\lambda + q_{t,0}\,, \tag{9}$$

and

$$q_z(\lambda) = \Upsilon_z\lambda + q_{z,0}\,, \tag{10}$$

where z is a new coordinate introduced, defined as

$$z := \cos\theta\,, \tag{11}$$

and Υ_t and Υ_z are the Mino time frequencies in the respective coordinates.

A full description of the analytical expressions relevant to this project is given in the Appendix B.

2.2 Calculating Impact Times

Assuming that the accretion disk lies along the entire equatorial plane of the primary, impacts of the secondary with the accretion disk are defined to occur when the polar angle value of the secondary black hole trajectory is $\theta = \pi/2$, or integer multiples thereof. The problem of calculating impact times then reduces to finding when the polar angle value of the secondary, θ, is an integer multiple of $\pi/2$, or equivalently when the z phase, q_z, is an integer multiple of π, since by convention $q_z = 0 \Rightarrow z = 0 \Rightarrow \theta = \pi/2$, as outlined by Van de Meent [12] and since we assume $q_{z,0} = 0$ in order to satisfy this requirement.

Another advantage of using Mino time to parameterise the equations of motion is that the radial coordinate solution and the polar angle solution are periodic in Mino time, such that

$$r(\lambda) = r(\lambda + n\Lambda_r)\,, \qquad \theta(\lambda) = \theta(\lambda + m\Lambda_\theta)\,, \tag{12}$$

where $\Lambda_{r,\theta}$ are the respective periodicities of the radial and polar angle solutions and n and m are integers. The periodicity of the polar angle, and thus the z coordinate, can be used to efficiently calculate the intersections with the accretion disk, corresponding to impact times.

Given that there are two impacts per orbit, we can calculate the Mino times of all impacts by taking integer multiples of half the polar period in Mino time, $\Lambda_\theta/2$, which corresponds to taking integer multiples of π divided the z frequency Υ_z, giving $n\pi/\Upsilon_z$, since the θ frequency and z frequency are equivalent. This is described mathematically as,

$$\int_{\theta=\pi/2}^{\theta=n\pi/2} d\lambda \equiv \frac{n\Lambda_\theta}{2} = \frac{n\pi}{\Upsilon_z} \,. \tag{13}$$

The corresponding coordinate times, $t = t(\lambda)$, of all impacts are then found using the integer multiples of π/Υ_z as Mino times,

$$t_{I,n} = t\left(\frac{n\pi}{\Upsilon_z}\right) , \qquad n \in \mathbb{Z} \,, \tag{14}$$

where $t_{I,n}$ is the coordinate time of the nth impact.

There exists, however, the issue of choosing a reference point which sets the initial coordinate time at $\lambda = 0$. We wish to have the first impact occur at $\lambda = 0$ so that integer multiples of π/Υ_z would correspond to all later impacts. However, we do not know *a priori* the coordinate time of the first impact since it is not observable; only the outbursts are. Therefore we choose $t_0 = t(0)$ to correspond to the time of the first well recorded outburst and then introduce a new *time shift* parameter, t_s, in order to shift our coordinate time at $\lambda = 0$ from the time of the first outburst to the time of the first impact.

Once shifted back, integer multiples of the half period can be taken to calculate all succeeding impacts. Although an estimation for t_s can be made, it is one of the parameters which we optimise for in the parameter estimation procedure. In order to remove the need to give an estimate for the initial temporal phase $q_{t,0}$, the difference between the nth impact and initial impact is taken, along with subtracting the time shift. The coordinate time of the nth impact is thus given as

$$t_{I,n} = \left[t\left(\frac{n\pi}{\Upsilon_z}\right) - t(0)\right] - t_s \,, \qquad n \in \mathbb{Z} \,. \tag{15}$$

All radii of impact can then be calculated in a similar fashion, by substituting integer multiples of π/Υ_z into equation (6).

Note that the coordinate times given in equation (15) are given in geometrised units. The total mass of the system M is required to convert these quantities to more transparent units, such as years. Therefore the total mass is required to predict the outburst times. This mass is one of the parameters which is optimised for in the parameter estimation algorithm.

2.3 Contrast and Justification

The use of Kerr geodesics to model the trajectory of the secondary black hole differs from previous efforts to model the OJ 287 system. Dey et al. have made use of PN expansions which are general relativistic corrections to Newtonian orbits in powers of $(v/c)^2$. The advantage of using PN expressions is that the mass of the secondary can be accounted and optimised for, along with radiation reaction emissions and the spin of the secondary mass. The disadvantage, however, is that PN expansions are not well suited to describe strong field dynamics. The highly eccentric orbit of the secondary black hole leads the trajectory into the strong gravitational field of the primary, suggesting that techniques which better account for strong field dynamics be used. Although the geodesic equations do not account for the mass nor the spin of the secondary black, they are fully strong-field. The effect of the secondary mass on the trajectory may also be neglected since we assume a large mass ratio between the primary and secondary. This means that the true orbit should deviate only slightly from a geodesic.

We also believe that the inclusion of radiation-reaction terms to account for the decay of the orbital constants due to gravitational wave emission is not fully necessary to accurately describe the orbit at this stage in its evolution and over a span of ∼100 years. Previous estimates have placed the merger of the two black holes to occur in about $10,000$ years [7], which, even if slightly inaccurate, should still be long enough to justify not accounting for the decay of the orbital constants, although this may be a point worth investigating further.

These points lead us to be confident that Kerr geodesics can accurately model the trajectory of the secondary black hole at this stage in its orbital evolution, over the given time-span of well observed outbursts.

3 Accretion Disk and Time Delays

3.1 Background

In this section, we examine how the accretion disk and corresponding time delays can be incorporated in our model. This is included in the work of Dey et al. via a formula derived in full detail in [13]. The basic idea of the derivation is that as the secondary black hole impacts the accretion disk of the primary, it causes a bubble of plasma to form that surrounds the radiation released from the impact. By using various assumptions, such as the impact occurring in the radiation pressure dominated region of the disk and that the bubble expands at the speed of sound in the disk, one can obtain an ODE in terms of the radial expansion rate of the bubble $\dot{R}$, which can be solved to give the radial evolution $R(t)$. It is then claimed that the bubble will become optically thin when it expands by a factor $\tau^{4/7}$, where τ is the effective optical depth of the bubble, at which time the radiation will be able to escape. Thus, by setting the expansion factor $R(t)/R_0$ equal to $\tau^{4/7}$ and using the previously obtained solution for $R(t)$, one obtains an equation for the time delay between impact and outburst, which has solution

$$t_d = d \cdot h^{13/21} n^{51/56} r_{\text{imp}}^{355/168} \tag{16}$$

where h is the disk semi - height at impact, n is the disk number density at impact, r_{imp} is the radius of impact and d is a constant. Note that the original equation in [13] contains a factor involving the mass of the secondary, however as we consider only the total mass of the system without taking into account the individual masses of the primary and secondary, we choose to absorb this into the proportionality constant d.

3.2 Introducing Randomness

The starting point for our model is the equation (16), which we develop further by choosing a particular model for the accretion disk. We opt for the standard Shakura - Sunyaev/α disk model ([14]), which is characterised by a viscosity parameter α ranging between 0 and 1, that quantifies the relationship between viscous stresses and pressure in the disk;

$$\tau_{r\theta} = \alpha P \tag{17}$$

with $\tau_{r\theta}$ the nonzero component of the viscous stress tensor in the disk, and P the total pressure. It is at this point we consider making a modification to the model of Dey et al., by introducing an element of randomness into the system, allowing us to use statistical methods for the parameter estimation process. We introduce this randomness in our model through the accretion disk. Accretion disks are known to be highly complex objects, in which chaotic processes such as turbulence contribute to seemingly random variability in their observed spectra (see [15], for a specific discussion of OJ 287 see [16]). For the Shakura - Sunyaev disk, this variability has been modelled in the literature through what is known as the *theory of propagating fluctuations*, first proposed by Lyubarskii in [17]. The primary concept of this model is that the viscosity parameter α is now treated as a stochastically varying quantity that induces randomness in the disk properties such as luminosity L and accretion rate $\dot{m}$ ([18],[19]). We choose to adopt this theory in our model in the following manner; making the same assumption as the Dey et al. model that the impacts happen in the radiation pressure dominated region of the disk, we obtain from the Shakura - Sunyaev model the following expressions for h and n as functions of the radius and disk properties;

$$h(r) \sim \dot{m}(1 - r^{-1/2}) \tag{18}$$

$$n(r) \sim \frac{r^{3/2}}{\alpha \dot{m}^2}(1 - r^{-1/2})^{-2} \tag{19}$$

Now if we incorporate the propagating fluctuations model, the accretion rate $\dot{m}$ becomes a *random variable* $\dot{M}$, which means both h and n, and hence the time delay itself t_d will become random variables H, N and T_d, with

$$T_d = d \cdot r_{\text{imp}}^{355/168} H^{13/21} N^{51/56} \tag{20}$$

which, upon using the expressions from (18) and (19), has expected value

$$\begin{aligned} \mathbb{E}[T_d] = C \cdot r_{\text{imp}}^{355/168}[1 - r_{\text{imp}}^{-1/2}]^{13/21} \\ \times [r_{\text{imp}}^{3/2}(1 - r_{\text{imp}}^{-1/2})^{-2}]^{51/56} \end{aligned} \tag{21}$$

where now C is a constant that absorbs the original constant d along with constants arising from the relationships in (18) and 19 and expectations of various powers of α and $\dot{M}$ (assuming that these are constant). This expression is convenient as it allows us to determine the expected value of each time delay purely from our orbit solution (which provides r_{imp}) up to the constant C, which is to be included in the parameter estimation process in later sections.

Note that, although we can straightforwardly find an expression for the expectation of our time delay random variable, the same cannot be said for its variance. This must be taken as a somewhat free parameter in the model that quantifies how much one wants to allow random fluctuations in the accretion disk to affect the time delay. We found taking $\text{Var}[T_d] \sim 0.01$ yr was both a reasonable and effective assumption to make for our model, as it leads to a standard deviation on each time delay of order 1 month (about 10% of the average expected time delay) and also ensures that each observed outburst time lies within at most 3 standard deviations of its expected value using our best parameter estimates found in later sections. It is also worth noting that we do not consider the time advance factor included in the model of Dey et al., and assume that the dominant contribution to the time difference between impact and outburst is the time delay.

3.3 A Statistical Model

Having established the random nature of each time delay using the propagating fluctuations model, we now look to build a statistical model for the observed outburst times that we can use to perform statistical inference on the parameters of the system. Central to this is the construction of a *likelihood function*, which is a measure of how likely our data set was to be observed as a function of the model parameters. This requires a probability density function for the time delays, which means we must specify a probability distribution that they follow. Now it is shown in [18] and [19] that the quantities α and $\dot{M}$ can be well modelled by what are known as *log - normal* probability distributions, for which the probability density function is

$$f_X(x) = \frac{1}{x\sqrt{2\pi\sigma^2}} \exp\left(-\frac{1}{2}\frac{[\ln x - \mu]^2}{\sigma^2}\right) \quad (22)$$

where μ and σ are parameters of the distribution defined by

$$\mu = \ln\left(\frac{\mathbb{E}[X]^2}{\sqrt{\mathrm{Var}[X] + \mathbb{E}[X]^2}}\right) \quad (23)$$

$$\sigma^2 = \ln\left(1 + \frac{\mathrm{Var}[X]}{\mathbb{E}[X]^2}\right) \quad (24)$$

This parametrisation is the one generally used as the definition of a log - normal variable is one whose logarithm is normally distributed, thus it is more convenient to parametrise by the mean and variance of the underlying normal (μ and σ^2). Now taking these quantities to follow log - normal distributions, and given the standard result that products and powers of log - normal random variables are still log - normal, it is clear that H, N, and hence T_d will follow log - normal distributions. Therefore, taking the ith time delay to be log - normal, and using the fact that $T_d^{(i)} = T_O^{(i)} - t_I^{(i)}$ where $T_O^{(i)}$ and $t_I^{(i)}$ are the ith (random) outburst and (deterministic) impact respectively, we find the pdf of the ith outburst as a function of the model parameters $\boldsymbol{\theta}$ as

$$\begin{aligned} f_{T_O^{(i)}}(t_O^{(i)}|\boldsymbol{\theta}) &= \frac{1}{[t_O^{(i)} - t_I^{(i)}(\boldsymbol{\theta})]\sqrt{2\pi\sigma^{(i)}(\boldsymbol{\theta})^2}} \\ &\times \exp\left(-\frac{1}{2}\frac{[\ln[t_O^{(i)} - t_I^{(i)}(\boldsymbol{\theta})] - \mu^{(i)}(\boldsymbol{\theta})]^2}{\sigma^{(i)}(\boldsymbol{\theta})^2}\right) \end{aligned} \quad (25)$$

Meaning the likelihood function for the 11 observed outbursts is given by, assuming independent time delays,

$$\begin{aligned} \mathcal{L}(\boldsymbol{T}_O|\boldsymbol{\theta}) &:= f_{\boldsymbol{T}_O}(\boldsymbol{t}_O|\boldsymbol{\theta}) \\ &= \prod_{i=1}^{11} f_{T_O^{(i)}}(t_O^{(i)}|\boldsymbol{\theta}) \end{aligned} \quad (26)$$

where the expression for the marginal densities is as in (25) and $\boldsymbol{T}_O$ is the vector of outburst times (with realisation $\boldsymbol{t}_O$). A graphic illustrating the concept of log - normally distributed time delays is included in Figure 3.

At this point it is worth noting that although there have been only 11 well observed outbursts of the OJ 287 system (given in Table 1), the approximate 12 year periodicity of the lightcurve in the better documented recent years suggests that there were further, unobserved outbursts of

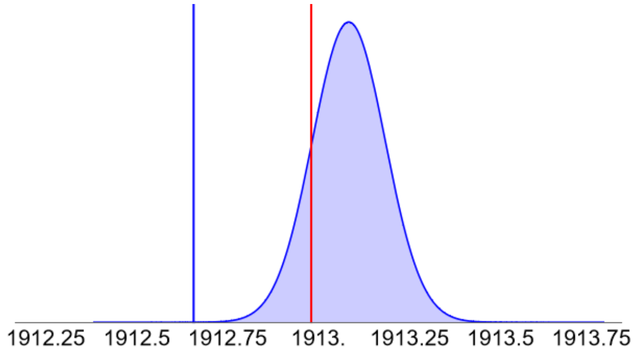

Figure 3: Example of a log-normally distributed time delay. Impact denoted by the blue line and observation by the red line.

the system earlier in the 20th century that went unnoticed for various reasons. Thus, any sensible model for computing impact times will have impacts in this time period that do not correspond to any observed outburst. These are not to be included in the likelihood function (26), as only impacts corresponding to actual observed data points make a contribution to the likelihood that the given outbursts were observed. Thus, certain impact times must be removed from the list $\boldsymbol{t}_I$. The correct impacts to remove were found by computing a set of impact times with the initial Keplerian/1PN estimates derived later in Section 5, and observing which elements in the list could have corresponded to observed outbursts. It is only these that are kept for use in the likelihood function.

It is also worth noting that the expression given for the likelihood function in equation (26) is in similar form to that used in gravitational wave parameter estimation, for example in [20], the difference being that our model assumes log - normally distributed observations, whereas for gravitational waves observations are usually assumed to be normally distributed.

4 Parameter Estimation

Having introduced a statistical model for our system, we can now use it to perform inference on our model parameters, the vector $\boldsymbol{\theta} = (p, e, M, q_{r,0}, t_s, C)$, where all quantities have been defined in previous sections. Note that we do not include the orbital parameters a (the spin of the primary) and $\theta_{\min}$ (the minimum polar angle of the orbit) in our parameter estimation algorithm. This is because these terms can be shown to have a sub - leading order effect on the dynamics, and we choose only to include leading order terms in our procedure in order to limit the dimension of parameter space for our estimation algorithms. In reality however, these terms can have a somewhat considerable effect on the orbit and so any in any potential future work it would be desirable to include them as parameters to be estimated. In this project, we took the value of the spin estimated by Dey et al. in [7] of $a = 0.381$, and, as in their work, the orbit to be almost perpendicular to the accretion disk, so $\theta_{\min} \sim 5\,\text{deg}$.

Now we wish to use a Bayesian approach to parameter estimation, deriving posterior densities $\pi(\boldsymbol{\theta})$ rather than point estimates for our parameters using Bayes' theorem;

$$\pi(\boldsymbol{\theta}|\boldsymbol{T}_O) = \frac{\mathcal{L}(\boldsymbol{T}_O|\boldsymbol{\theta})p(\boldsymbol{\theta})}{Z} \tag{27}$$

where $p(\boldsymbol{\theta})$ is the prior distribution of our parameters, which expresses our initial beliefs about their values, and Z is a normalisation factor known as the 'evidence', required to ensure that $\int \pi(\boldsymbol{\theta}|\boldsymbol{T}_O)d\boldsymbol{\theta} = 1$. Our parameter estimates and associated uncertainties can then be found by computing moments of the posterior distribution. Now for our problem, as is often the case in Bayesian inference, it is not possible to obtain the evidence in a closed form. Thus, rather than obtaining the posterior directly, we must use computational techniques to *sample* from it, in order to approximate its distribution and moments. A further issue for our model is that the posterior density itself is quite irregular as it only has support on regions of parameter space that give impact times occurring *before* the observed outbursts (due to the log - normal distribution of the time delay only having support on the positive real line), meaning we will have to follow a careful procedure to make sampling from it tractable. This procedure consists of three main steps;

1. Use astronomical observations along with Keplerian/1PN formulae to obtain rough initial guesses for our parameters
2. Use a numerical optimisation technique to obtain the approximate dominant mode of the posterior distribution
3. Implement a sampling algorithm (that does not require knowledge of Z) initialised from the posterior mode found in step 2. to compute approximate moments of the posterior for parameter estimation

(Note that steps 2. and 3. follow the procedure suggested in [21] for sampling from a complicated posterior). We now expound on each of these steps in further detail.

4.1 Initial Keplerian/1PN Estimates

As mentioned in previous sections, the light curve of OJ 287 contains important information about the system - perhaps most importantly, it gives that the system exhibits an orbital (quasi) period T of approximately 12 years, a precessional period of approximately 120 years, and that the eccentricity of the elliptical orbit must be about 0.7 ([1]). From this, one can glean a surprising amount of information about the system, as shown in [1]. Firstly, the precessional period of 120 years means that the system exhibits a perihelion precession $\Delta\phi$ of approximately $12 \cdot \frac{360}{120} =$ 36 degrees per orbit. Next, if we combine Kepler's third law

$$T^2 = \frac{4\pi^2 a^3}{GM} \tag{28}$$

with the 1PN expression for perihelion precession per orbit

$$\Delta\phi = \frac{6\pi GM}{c^2 a(1-e^2)} \tag{29}$$

by eliminating the semi major axis a, we obtain the following expression giving a rough estimate for the total mass of the system;

$$M = \frac{c^3 \Delta\phi^{3/2}(1-e^2)^{3/2} T}{12\sqrt{6} G \pi^{5/2}} \tag{30}$$

(Note that (30) gives an overestimation of the mass, as higher order PN terms cause additional positive contributions to the right hand side of (29)). From this estimate for the mass, we may rearrange (28) to give an estimate for the semi - major axis, which in turn provides us with an initial estimate for the semi - latus rectum p via the formula

$$p = a(1-e^2) \tag{31}$$

The solutions given in Section 2 are 2π periodic in the radial phase q_r, thus we constrain the initial radial phase $q_{r,0}$ to range between 0 and 2π, meaning the only requirement on an initial guess for this parameter is that it lies in this interval. We choose as our initial guess $q_{r,0} = \pi$, simply because it is the midpoint of this interval. We then obtain an order of magnitude initial estimate for the constant C by requiring the average expected time delay to be of order ~ 1 year, to be somewhat consistent with the previous work of Dey et al. in, for example, [7] (where we have taken C to be in units so that the expected time delay is in years). This is done by averaging the expression (21) from periapsis to apoapsis using integration and finding the order of magnitude of C required to make this time delay $O(1)$ year. Finally, the initial guess for the time shift t_s is simply found as the expected time delay for an impact occurring at the initial radial coordinate $r(0)$ using (21). Thus, we have approximate initial guesses for each of our model parameters, and may use these as a starting point for the next step in our parameter estimation algorithm.

4.2 Optimisation Step - Simulated Annealing

4.2.1 Outline of the Algorithm

The next step in the process is to locate the dominant posterior mode via a numerical optimisation algorithm. The choice of algorithm here is crucial as the expression for the posterior density is complex, with many small, local maxima, and thus an algorithm which simply uses local information to flow to maxima such as gradient descent will not be sufficient, as it will continually get stuck in these local extrema.

What we need instead is an algorithm that can perform a much wider search of the parameter space, that won't encounter this problem of getting stuck locally, and will be able to find approximate *global* maxima of the posterior. Thus, an appropriate choice is the probabilistic optimisation metaheuristic known as *simulated annealing*, first proposed by Kirkpatrick in [22]. This technique was originally inspired by the procedure of annealing in metallurgy, where a metal is slowly cooled in order to change its structural properties such as ductility and hardness.

The key idea of the algorithm is that there is an 'energy' function that one wants to minimise by randomly exploring different 'states' in parameter space. Proposed states are accepted or rejected based on a 'temperature' parameter, that decreases as the algorithm runs, with the probability of accepting a nonoptimal move becoming smaller and smaller as the temperature decreases.

This is analogous to the physical process of annealing - here the atoms in the metal want to arrange themselves so as to minimise the total energy of the system. At the beginning of the process, when the temperature is high, the system may accept moves to higher energy configuration with some probability, but this probability decreases with the temperature and so by the end the system will only accept moves to lower energy states. It is in this way that the total energy of the system is minimised. Importantly, from an optimisation perspective, this accepting of nonoptimal moves prevents the algorithm from becoming stuck in local minima, which allows a greater exploration of the search space.

In more detail, the algorithm proceeds as follows;

Simulated Annealing Algorithm

1. Begin with initial state $\boldsymbol{\theta}_0$ with energy E.
2. Propose a new state $\boldsymbol{\theta}_n$ with energy E_n randomly via a Gaussian centred at the current state.
3. Accept/reject $\boldsymbol{\theta}_n$ if the temperature - dependent probability

$$P(E, E_n, T) = \begin{cases} 1, & (E_n < E) \\ \exp(-\frac{E_n - E}{T}), & (E_n > E) \end{cases}$$

   is greater than/less than a randomly drawn number between 0 and 1.
4. Repeat for desired number of iterations, decreasing the temperature each time.

4.2.2 A Toy Problem - the Weierstrass Function

Having introduced the simulated annealing algorithm and discussed its appropriateness for our model, we now briefly consider a toy problem as a demonstration of its efficacy. We examine maximising the truncated Weierstrass function, given by

$$f(x) = \sum_{n=0}^{N} a^n \cos\left(b^n \pi x\right) \tag{32}$$

We take $N = 2, a = 0.7$, and $b = 5$. Now this function has many local maxima which are easily found, the problem lies in finding its *global* maximum, located at $x = 0$. We can solve this problem by applying simulated annealing, with energy given by $-f$ (so that we are maximising f). Figure 4 shows how the algorithm zeroes in on the global maximum by randomly exploring the search space, accepting nonoptimal moves at higher temperatures to avoid getting stuck in one of the many local maxima.

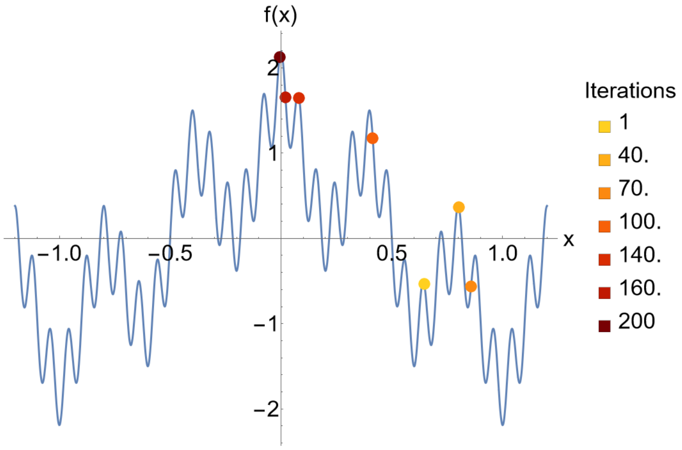

Figure 4: Optimising the truncated Weierstrass function using Simulated Annealing. The algorithm explores the search space stochastically and finds the approximate global maximum as the temperature cools.

The details of how simulated annealing was used to locate the posterior mode for our problem is discussed in more detail in Section 5.

4.3 Sampling Step - Metropolis Hastings

4.3.1 Outline of the Algorithm

We now consider the final step in the procedure, sampling from the posterior distribution. As mentioned already, we cannot obtain the posterior distribution in closed form due to the normalisation constant. Thus, we instead opt for an algorithm that can sample from this distribution, allowing us to compute approximations to its moments which we will use for parameter estimation. One such family of algorithms is what is known as *Markov Chain Monte Carlo*, or *MCMC* methods.

These techniques involve constructing a Markov chain of samples whose stationary distribution is the desired posterior distribution. One can then compute estimations for the moments using the Monte Carlo approximation ([23]). Further, many MCMC algorithms do not require knowledge of a normalisation factor to sample from a distribution, and need only a function *proportional to* the desired pdf. This makes them ideally suited for our problem.

We choose one such algorithm, the simplest and most widely used example of MCMC, known as the *Metropolis - Hastings* algorithm, first developed in [24]. The general structure of the algorithm is very similar to the previously discussed simulated annealing - in fact, Metropolis - Hastings was essentially what inspired the development of simulated annealing, with the latter being a version of the former adapted to optimisation problems rather than sampling.

As in simulated annealing, proposed states are accepted/rejected based on a criteria that always accepts optimal moves (in this case, moves to regions of higher probability density) but has a nonzero probability of accepting nonoptimal ones to avoid getting stuck in local maxima. The primary difference is that in Metropolis - Hastings, each accepted state is recorded and viewed as a sample from the desired distribution, whereas in simulated annealing, the only state that is recorded is the one that best minimises the energy function. In more detail, the algorithm proceeds as follows;

Metropolis - Hastings Algorithm

1. Begin with initial sample $\boldsymbol{\theta}^{(0)}$ and propose $\boldsymbol{\theta}'$ via a multivariate Gaussian centred at $\boldsymbol{\theta}^{(0)}$.

2. Accept or reject $\boldsymbol{\theta}'$ as new sample $\boldsymbol{\theta}^{(1)}$ if the ratio

   $$r = \min\left(1, \frac{\pi(\boldsymbol{\theta}')}{\pi(\boldsymbol{\theta}^{(0)})}\right)$$

   is greater than/less than a randomly drawn number between 0 and 1.

3. Repeat for N iterations and approximate moments using the Monte Carlo formula

   $$\mathbb{E}_{\pi}[g(\boldsymbol{\theta})] \simeq \frac{1}{N}\sum_{n=1}^{N} g(\boldsymbol{\theta}^{(n)})$$

Note that, as the acceptance criteria depends only on *ratios* of posterior densities, the normalisation constant completely cancels and so no knowledge of it is needed to perform the sampling. The formula in Step 3. is based on the Monte Carlo principle that probability distributions and their associated moments can be well approximated by repeated random sampling and averaging over these samples. It is also worth noting that usually these sums are not performed over all samples, with a certain fraction of the initial samples ignored in what is known as a 'burn - in' phase, to allow the algorithm time to explore the posterior and locate regions of higher density. We essentially bypass the need for this burn in time by our previously discussed optimisation step, which immediately places the sampler in a region of high posterior density.

4.3.2 A Toy Problem - Sampling from an $\mathcal{N}(0,1)$ Distribution

We now briefly discuss another toy problem to demonstrate the operation of the Metropolis - Hastings algorithm. We consider the problem of sampling from an $\mathcal{N}(0,1)$ distribution *without* knowledge of the normalisation constant - in other words knowing only that

$$f_X(x) \propto \exp\left(-\frac{1}{2}x^2\right) \tag{33}$$

We also compute the Monte Carlo estimates for the mean and variance of the distribution;

$$\begin{aligned} \hat{\mu} &= \frac{1}{N}\sum_{n=1}^{N} x_n \\ \hat{\sigma}^2 &= \frac{1}{N}\sum_{n=1}^{N}(x_n - \hat{\mu})^2 \end{aligned} \tag{34}$$

where the x_n are the samples drawn using the algorithm. The results are included in Figure 5. It can be seen that both the sampling distribution and parameter estimates give reasonable approximations that increase in accuracy as the number of iterations N is increased.

Again, the details of how this algorithm is applied to our problem are discussed in the next section.

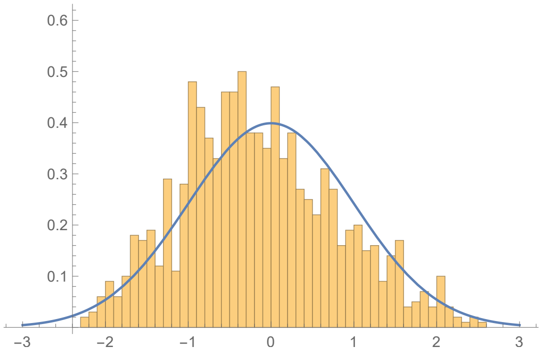

(a) 1000 iterations. $\hat{\mu} \simeq -0.14$, $\hat{\sigma}^2 \simeq 0.89$.

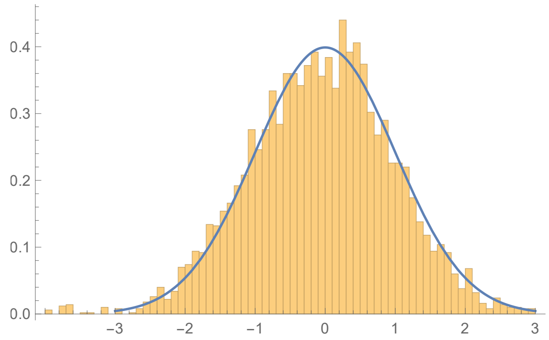

(b) 5000 iterations. $\hat{\mu} \simeq -0.06$, $\hat{\sigma}^2 \simeq 1.03$

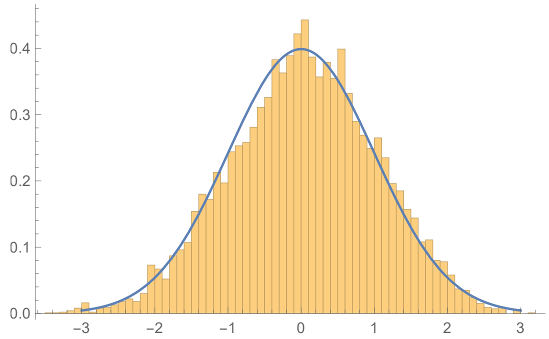

(c) 10000 iterations. $\hat{\mu} \simeq 0.04$, $\hat{\sigma}^2 \simeq 0.997$.

Figure 5: Sampling from an $\mathcal{N}(0,1)$ distribution for sample sizes of $1,000$, $5,000$ and $10,000$. The accuracy of the computed moments increases as the sample size increases.

It is worth noting that our sampling procedure involves locating the posterior mode and exploring the surrounding region using the Metropolis - Hastings algorithm. This idea works well for a unimodal posterior but in reality, our posterior is highly irregular and is in fact multimodal which may lead to doubts regarding the accuracy of this procedure for sampling from it. Our claim however is that, although there are many local maxima of the distribution, there is one dominant mode corresponding to a global maximum where an overwhelming majority of the posterior density resides (around the ‘true’ parameters of the system). This claim is supported by results found by the simulated annealing algorithm - there were many small, local maxima located in parameter space but comparing to the global maximum found, the ratio of densities in these regions was generally found to be $\sim O(10^{-4})$. Thus, we believe that treating this distribution as essentially unimodal offers a reasonable approximation, with regions away from this mode contributing very little to the integrals that give moments of the distribution. This means that the resulting Monte Carlo approximations of the moments should give satisfactory estimates for the parameters and their uncertainties. More work is needed however to investigate the validity of this approximation.

5 Results

In this section we present the results obtained from the procedure discussed previously. All code used to produce these results was implemented in MATHEMATICA.

The first aspect to consider is the Keplerian/1PN initial parameter estimates. If we plug $T = 12\text{yr}$, $\Delta\phi = 36\,\text{deg}$, $e = 0.7$ into (30), we obtain $M \simeq 27 \times 10^9 M_\odot$. Recall however that this is an overestimate of the mass, and we cannot be sure of how much an overestimate this is. Thus rather than taking this value to start our optimisation step, we take a range of values of the mass lower than this, and run our optimisation step from each one. We took three values, $M = 24$, 25 and $26 \times 10^9 M_\odot$ which had corresponding semi - latus rectums of approximately $p = 33$, 32 and 31 respectively, calculated via (31). We have stated already that the initial guess for $q_{r,0}$ was π, and the order of magnitude estimate for C was found to be $\sim 10^{-7}$. This gave an initial guess for t_s of approximately 1yr. Thus we obtain three sets of rough initial parameter estimates, $\boldsymbol{\theta}_0 = (33/32/31, 0.7, 24/25/26, \pi, 1, 1)$, which we use as starting points for our optimisation step (note that here and from now on, the masses are taken to be in billions of solar masses and C in units of 10^{-7}).

With these values in mind, we take the prior distributions on our parameters p, e, M, $q_{r,0}$, t_s and C to be uniform on the intervals $[31, 35]$, $[0, 1]$, $[23, 27]$, $[0, 2\pi]$, $[0, 12]$ and $[0, 10]$, respectively. These ranges for p and M are chosen so that they lie in the immediate regions above/below the under/overestimates found above. The ranges for e and $q_{r,0}$ are so since they span the full range of possible values for these parameters. The range for t_s is constrained by the 12 year orbital quasi-period, and C by its order of magnitude estimate made previously.

Having found rough initial parameter estimates, we run simulated annealing with these as our initial state $\boldsymbol{\theta}_0$, taking the energy to be the negative of the numerator of the posterior from (27). As mentioned previously, new states in parameter space are proposed via a Gaussian centred at the current state. At this stage, rather than employing a multivariate Gaussian for this purpose, a single element of the state is chosen at random and a univariate Gaussian centred at this element, with some user specified variance, is used to propose a new state. The algorithm was implemented by running 500 iterations from the initial guesses, taking the output of this run, and using this as a new initial state for another 500 iteration run, decreasing the variance of the Gaussian proposal distribution to more narrowly probe this region of parameter space. This process was repeated until the algorithm no longer improved on the initial guess, suggesting an approximation to the true global maximum of the posterior had been found. The best values found by this procedure (i.e. the ones that best minimised the energy) were, to three significant figures, $\boldsymbol{\theta} = (32.2, 0.688, 24.4, 2.38, 0.262, 1.95)$.

The posterior mode found by simulated annealing can then be used to initialise the Metropolis - Hastings sampling step. Here, we modify our procedure for generating new samples. The proposal distribution is now taken to be a multivariate Gaussian centred at the current state. The covariance matrix of the proposal is determined using a procedure suggested in [21] - a short run of the Metropolis - Hastings algorithm of about 500 iterations is performed with a diagonal covariance matrix, and the covariance of the resulting samples is calculated and taken to be the new proposal covariance. This procedure can be repeated until a covariance matrix that gives a satisfactory acceptance rate is achieved, and this will then be used for the full Metropolis - Hastings run. Having found such a covariance matrix through this procedure, we then ran the algorithm for $N = 10,000$ iterations to obtain samples from the posterior distribution. We took as our parameter estimates the Monte Carlo means of these samples (approximating the minimum mean squared error, or MMSE estimator), and as our uncertainties the Monte Carlo standard deviations;

$$\begin{aligned}
\hat{\boldsymbol{\theta}} &= \mathbb{E}_\pi[\boldsymbol{\theta}|\boldsymbol{T}_O] \\
&\simeq \frac{1}{N}\sum_{n=1}^{N} \boldsymbol{\theta}^{(n)} \\
\hat{\boldsymbol{\sigma}} &= \sqrt{\mathbb{E}_\pi\left[(\boldsymbol{\theta} - \mathbb{E}_\pi[\boldsymbol{\theta}|\boldsymbol{T}_O])\,|\boldsymbol{T}_O\right]} \\
&\simeq \sqrt{\frac{1}{N}\sum_{n=1}^{N}\left(\boldsymbol{\theta}^{(n)} - \hat{\boldsymbol{\theta}}\right)^2}
\end{aligned} \tag{35}$$

The results are included in Table 2.

Parameter	Estimates	
p	32.1	±0.06
e	0.687	±0.001
M	24.4	±0.1
$q_{r,0}$	2.36	±0.03
t_s	0.32	±0.07
C	2.2	±0.3

Table 2: Estimates for the parameters with 1σ uncertainties of OJ 287 from Metropolis - Hastings.

It is worth noting that the mass in our estimates is measured as an observer on Earth, whereas the estimates of Dey et al. are in the frame of the OJ 287 system itself. To convert our estimates for comparison, we must simply divide by $1+z$, where the redshift factor $z = 0.306$. This gives our estimate as $\sim 18.7 \times 10^9 M_\odot$, while the estimate of Dey et al. was $\sim 18.5 \times 10^9 M_\odot$ - which is within two of the computed standard deviations of our result, indicative of a reasonable agreement.

Finally, we present the expected outburst times as predicted by our model with the observed data in Table 3, along with a visual representation of the outbursts given in Figure 6, where each vertical red line denotes an observed outburst and blue an expected outburst as calculated by our model. We emphasise that these are *expected* outbursts predicted by our model, when each of the time delay random variables take their expected values. Our model however gives that they can deviate from this due to random processes in the accretion disk, which offers some explanation for the disagreements in the table.

Outburst Times						
Observed	1912.98	1947.28	1957.01	1972.94	1982.97	1984.13
Expected	1913.08	1947.29	1956.82	1972.8	1982.95	1984.03
Abs. Difference	0.1	0.01	0.19	0.14	0.02	0.1
Observed	1995.84	2005.75	2007.69	2015.88	2019.57	
Expected	1995.78	2005.96	2007.66	2016.02	2019.58	
Abs. Difference	0.06	0.21	0.03	0.14	0.01	

Table 3: Observed and expected outburst times with their differences, starting from the year 1912.980. Recall that the standard deviation of the outbursts was taken to be 0.1 years.

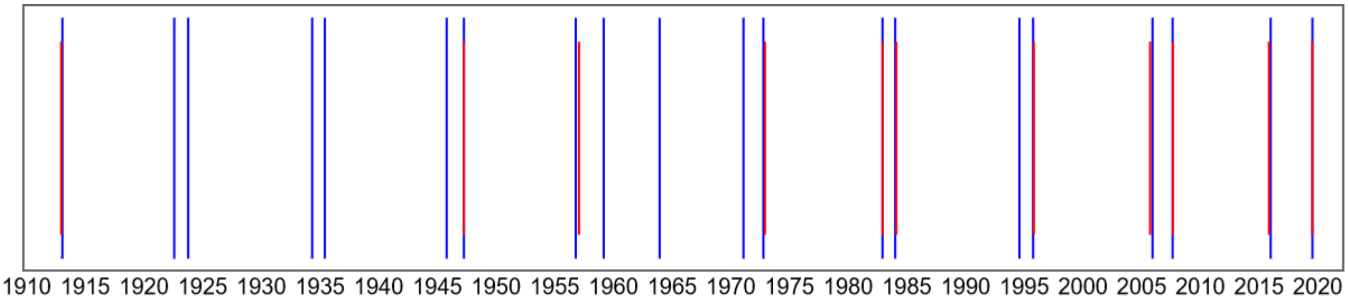

Figure 6: Expected and observed outburst times, with expected in blue and observed in red. The close overlap between the blue and red lines indicates good agreement of our model with observations. Recall that, for a variety of reasons, outbursts may not have been observed, corresponding to blue lines with no accompanying red one.

6 Conclusion

In this project, we have developed a framework for applying techniques of Bayesian inference to estimate the parameters of the OJ 287 system. We have approached this by modelling the motion of the SMBBH system using Kerr geodesics, making use of the analytical solutions available to find impact times of the secondary with the accretion disk in a computationally efficient way. We then introduced randomness into the system through these impacts, taking the deterministic time delay formula of previous models and treating this as an expected value of a log - normally distributed random variable, which arises due to stochastic processes in the accretion disk. This allowed us to build a statistical model for the outburst times, to which we applied Bayesian methods to obtain estimates for the parameters along with uncertainties. These parameters produced a set of expected outburst times which we compared to previous observations, and also to make predictions about future outbursts from the system. We found a reasonably good agreement between the expected results of our model and the previously observed outbursts, with an average absolute difference of approximately 1 month. We also predict the next three outbursts to occur in 2022.7, 2031.47 and 2032.81. The first of these corresponds to some time in August 2022, however this is unlikely to be observed as the OJ 287 system is currently behind the Sun. There are, however, significant improvements that can still be made to the model. Firstly, it would be useful to investigate the impact of including mass ratio terms and radiation reaction effects in the equations of motion on the parameter estimates and corresponding outburst times, and also comparing the motion of the secondary modelled by geodesics to the PN formalism employed by Dey et al.. Further, it would be of interest to investigate the effect of approximating the posterior as unimodal by including MCMC runs initialised at a number of different local maxima and seeing the impact this had on the parameter estimates and the associated uncertainties. Alternatively, one could attempt to fit a different, more regular distribution than a log - normal (for example a normal) to the time delays which could mitigate this issue by improving the regularity of the posterior. Finally, a thorough examination of the convergence of the Metropolis - Hastings algorithm would be desirable to support the obtained results and offer confirmation of the validity of the method for this problem.

Appendix A: The Orbital Constants of Motion

The geodesic equations are given in terms of the parameters $(\mathcal{E}, \mathcal{L}_z, \mathcal{Q})$, corresponding to the energy, the axial angular momentum and Carter's constant, however, Schmidt derived the relationship between these constants and the more convenient $(p, e, \theta_{\min})$ [10]. The aim is to present candidate orbits using the $(p, e, \theta_{\min})$ parameterisation, then find the corresponding values of $(\mathcal{E}, \mathcal{L}_z, \mathcal{Q})$ such that the Kerr geodesic equations can be calculated.

It is worth noting that the values of $\mathcal{E}$, $\mathcal{L}_z$ and $\mathcal{Q}$ used in the geodesic equations are dimensionless quantities. They are written without additional notation in order to keep the notation simple, however in this derivation a tilde is added to the symbol to denote that it is dimensionless.

We can relate the dimensionful quantities to their dimensionless counterparts with $\mathcal{E} = \mu\tilde{\mathcal{E}}$, $\mathcal{L}_z = \mu M \tilde{\mathcal{L}}_z$ and $\mathcal{Q} = (\mu M)^2 \tilde{\mathcal{Q}}$, where M is the mass of the primary and μ the mass of the test particle. Given a minimum orbital radius r_1 and a maximum radius r_2, where $r_1 = p/(1+e)$ and $r_2 = p/(1-e)$, we can relate the constants with the following equations. Note that $D = \text{sgn}\mathcal{L}_z$ and specifies whether the orbit is prograde or retrograde, given $D = +1$ or $D = -1$ respectively.

$$\tilde{\mathcal{E}}^2 = \frac{\kappa\rho + 2\epsilon\sigma - 2D\sqrt{\sigma(\sigma\epsilon^2 + \rho\epsilon\kappa - \eta\kappa^2)}}{\rho^2 + 4\eta\sigma}\,, \tag{36}$$

$$\tilde{\mathcal{L}}_z = -\frac{g_1\tilde{\mathcal{E}}}{h_1} + D\sqrt{\frac{g_1^2\tilde{\mathcal{E}}^2}{h_1^2} + \frac{f_1\tilde{\mathcal{E}}^2 - d_1}{h_1}}\,, \tag{37}$$

$$\tilde{\mathcal{Q}} = z_-\left(\beta + \frac{\tilde{\mathcal{L}}_z^2}{1 - z_-}\right)\,, \tag{38}$$

where we define $\tilde{a} = a/M$, $z_- = \cos^2\theta_{\min}$ and $\beta = \tilde{a}^2(1 - \tilde{\mathcal{E}}^2)$, with the functions

$$\tilde{\Delta}(\tilde{r}) = \tilde{r}^2 - 2\tilde{r} + \tilde{a}^2\,, \tag{39}$$

$$d(\tilde{r}) = (\tilde{r}^2 + z_-\tilde{a}^2)\tilde{\Delta}\,, \tag{40}$$

$$f(\tilde{r}) = \tilde{r}^4 + \tilde{a}^2(\tilde{r}(\tilde{r}+2) + z_-\tilde{\Delta})\,, \tag{41}$$

$$g(\tilde{r}) = 2\tilde{a}\tilde{r}\,, \tag{42}$$

$$h(\tilde{r}) = \tilde{r}(\tilde{r} - 2) + \frac{z_-\tilde{\Delta}}{1 - z_-}\,, \tag{43}$$

and the determinants

$$\kappa = d_1 h_1 - d_2 h_1\,, \tag{44}$$

$$\epsilon = d_1 g_2 - d_2 g_1\,, \tag{45}$$

$$\rho = f_1 h_2 - f_2 h_1\,, \tag{46}$$

$$\eta = f_1 g_2 - f_2 g_1\,, \tag{47}$$

$$\sigma = g_1 h_2 - g_2 h_1\,. \tag{48}$$

A subscript 1 or 2 means that the function should be evaluated at the dimensionless radius $\tilde{r}_{1,2}$.

In the Kerr equations of motion the dimensionless constants, $\tilde{\mathcal{E}}, \tilde{\mathcal{L}}_z$ and $\tilde{\mathcal{Q}}$, are used, however the tildes are removed for notational cleanliness.

Appendix B: Analytical Solution to Kerr Geodesic Equations

Organisation and Geodesic Equations

The Kerr geodesic equations of motion from Section 2.1 were solved analytically, when parameterised with Mino time, by Fujita and Hikida [11]. The solutions were organised and presently more compactly by Van de Meent [12] and are outlined in this appendix. The solutions are quite long and are thus defined in pieces in the pursuit of clarity. Although the full solutions to all the coordinates are provided by Van de Meent, only solutions to equations necessary to predict the expected outbursts of OJ 287 are used, namely the radial solution, r, and the coordinate time solution, t. The following solutions are given in geometrised units, where $G = c = 1$.

In first order form, the geodesic equations to be solved from Section 2.1 can be written as

$$\left(\frac{dr}{d\lambda}\right)^2 = (1-\mathcal{E}^2) \times (r_1 - r)(r - r_2)(r - r_3)(r - r_4)\,, \tag{49}$$

$$\left(\frac{dz}{d\lambda}\right)^2 = (z^2 - z_1^2)(a^2(1-\mathcal{E}^2)z^2 - z_2^2)\,, \tag{50}$$

$$\left(\frac{dt}{d\lambda}\right) = \frac{r^2+a^2}{r^2-2r+a^2}(\mathcal{E}(r^2+a^2) - a\mathcal{L}_z) - a^2\mathcal{E}(1-z^2) + a\mathcal{L}_z\,, \tag{51}$$

$$\left(\frac{d\phi}{d\lambda}\right) = \frac{a}{r^2-2r+a^2}(\mathcal{E}(r^2+a^2) - a\mathcal{L}_z) + \frac{\mathcal{L}_z}{1-z^2} - a\mathcal{E}\,, \tag{52}$$

where we have a new coordinate, z, defined as

$$z \coloneqq \cos(\theta) \tag{53}$$

which replaces the usual Boyer-Lindquist coordinate θ.

Initial Definitions

The first order Kerr geodesic equations are written in terms of roots of the r and z equations, defined to be

$$r_1 = \frac{p}{1-e}\,, \tag{54}$$

$$r_2 = \frac{p}{1+e}\,, \tag{55}$$

$$r_3 = \frac{1}{1-\mathcal{E}^2} - \frac{r_1+r_2}{2} + \sqrt{\left(\frac{r_1+r_2}{2} - \frac{1}{1-\mathcal{E}^2}\right)^2 - \frac{a^2\mathcal{Q}}{r_1 r_2(1-\mathcal{E}^2)}}\,, \tag{56}$$

$$r_4 = \frac{a^2\mathcal{Q}}{r_1 r_2 r_3 (1-\mathcal{E}^2)}\,, \tag{57}$$

and the z roots given as

$$z_1 = \cos(\theta_{\min}) \,, \tag{58}$$

$$z_2 = \sqrt{a^2(1-\mathcal{E}^2) + \frac{\mathcal{L}_z^2}{1-z_1^2}} \,. \tag{59}$$

The inner and outer event horizons are located at the radial coordinates

$$r_{\pm} = 1 \pm \sqrt{1-a^2}. \tag{60}$$

These definitions now allow the following relevant quantities to be defined;

$$k_r = \frac{(r_1-r_2)(r_3-r_4)}{(r_1-r_3)(r_2-r_4)} \,, \tag{61}$$

$$k_z = a^2(1-\mathcal{E}^2)\frac{z_1^2}{z_2^2} \,, \tag{62}$$

$$h_r = \frac{r_1-r_2}{r_1-r_3} \,, \tag{63}$$

$$h_{\pm} = h_r \frac{r_3-r_{\pm}}{r_2-r_{\pm}} \,. \tag{64}$$

The Radial Solution

The solution to the radial equation is given as

$$r(q_r) = \frac{r_3(r_1-r_2)\mathrm{sn}^2(\frac{K(k_r)}{\pi}q_r|k_r) - r_2(r_1-r_3)}{(r_1-r_2)\mathrm{sn}^2(\frac{K(k_r)}{\pi}q_r|k_r) - (r_1-r_3)} \,, \tag{65}$$

where sn is the Jacobi elliptic sine function and K is the complete Jacobi elliptic integral of the first kind.

The quantity q_r is the radial phase and is a secularly growing part of the solution which grows with Mino time, defined as

$$q_r(\lambda) = \Upsilon_r \lambda + q_{r,0} \,, \tag{66}$$

where Υ_r is the radial frequency and $q_{r,0}$ the initial radial phase. This gives the value of q_r at Mino time $\lambda = 0$ and corresponds to periapsis ($r = r_2$). Although an initial guess can be made for $q_{r,0}$, it is one of the parameters which is optimised for in the parameter searching algorithm in this project, since we would not know *a priori* what the initial radial phase of a trajectory is, without setting it arbitrarily.

The radial frequency is given as

$$\Upsilon_r = \frac{\pi}{2K(k_r)}\sqrt{(1-\mathcal{E}^2)(r_1-r_3)(r_2-r_4)} \,. \tag{67}$$

The Temporal Solution

Similarly, the solution to coordinate time is given as

$$t(q_t, q_r, q_z) = q_t + t_r(q_r) + t_z(q_z) \,, \tag{68}$$

which is a function of three phases, q_t, q_r and q_z.

The radial phase, q_r, has already been defined, while the z phase is given as

$$q_z = \Upsilon_z \lambda + q_{z,0} \tag{69}$$

where $q_{z,0}$ corresponds to the initial z phase which is the value of q_z at $\lambda = 0$. It is taken as convention here that $q_z = 0$ corresponds to the up-going node of the polar motion, i.e. $z = 0$, $z' > 0$. It is thus assumed in this project that this is the case and so $q_{z,0} = 0$.

The corresponding z frequency is given as

$$\Upsilon_z = \frac{\pi z_2}{2K(k_z)} \,. \tag{70}$$

Although not necessary in this project, the solution to the z is nonetheless given as

$$z(q_z) = z_1 \mathrm{sn}\left(K(k_z)\frac{2q_z}{\pi}|k_z\right) . \quad (71)$$

Once q_r and q_z can be calculated, they can be substituted into the expressions for t_r and t_z, given as

$$t_r(q_r) = \tilde{t}_r\left(\mathrm{am}\left(K(k_r)\frac{q_r}{\pi}|k_r\right)\right) - \frac{\tilde{t}_r(\pi)}{2\pi}q_r\,, \quad (72)$$

$$t_z(q_z) = \tilde{t}_z\left(\mathrm{am}\left(K(k_z)\frac{2q_z}{\pi}|k_z\right)\right) - \frac{\tilde{t}_z(\pi)}{\pi}q_z\,, \quad (73)$$

where

$$\begin{aligned}\tilde{t}_r(\zeta_r) = {} & \frac{\mathcal{E}(r_2-r_3)}{\sqrt{(1-\mathcal{E}^2)(r_1-r_3)(r_2-r_4)}} \\ & \times ((4+r_1+r_2+r_3+r_4)\Pi(h_r;\zeta_r|k_r) \\ & - \frac{4}{r_+-r_-}(\frac{r_+(4-a\mathcal{L}_z/\mathcal{E})-2a^2}{(r_2-r_+)(r_3-r_+)} \\ & \times \Pi(h_+;\zeta_r|k_r) - (+\leftrightarrow -)) \\ & + \frac{(r_1-r_3)(r_2-r_4)}{r_2-r_3} \\ & \times (E(\zeta_r|k_r) - h_r\frac{\sin\zeta_r\cos\zeta_r\sqrt{1-k_r\sin^2\zeta_r}}{1-h_r\sin^2\zeta_r})\,, \end{aligned} \quad (74)$$

and

$$\tilde{t}_z(\zeta_z) = -\frac{\mathcal{E}}{1-\mathcal{E}^2}z_2E(\zeta_z|k_z)\,, \quad (75)$$

where E and Π are elliptic integrals of the second and third kind, respectively. Also, the notation $(+\leftrightarrow -)$ indicates that the previous term is to be repeated again, however with the plus and minus signs in the subscripts swapped around.

Finally, our attention can be turned to the temporal phase, q_t, given as

$$q_t(\lambda) = \Upsilon_t\lambda + q_{t,0}\,. \quad (76)$$

We can however take $q_{t,0} = 0$ since we can absorb its effects into our time shift parameter t_s and optimise for it in the parameter estimation algorithm.

The associated frequency is given as

$$\Upsilon_t = \tilde{\Upsilon}_{t,r} + \tilde{\Upsilon}_{t,z}\,. \quad (77)$$

The relevant terms are defined as

$$\begin{aligned}\tilde{\Upsilon}_{t,r} = {} & (4+a^2)\mathcal{E} + \mathcal{E}\ (\frac{1}{2}((4+r_1+r_2+r_3)r_3 \\ & - r_1r_2 + (r_1-r_3)(r_2-r_4)\frac{E(k_r)}{K(k_r)} \\ & + (4+r_1+r_2+r_3+r_4)(r_2-r_3)\frac{\Pi(h_r|k_r)}{K(k_r)}) \\ & + \frac{2}{r_+-r_-}(\frac{(4-a\mathcal{L}_z/\mathcal{E})r_+-2a^2}{r_3-r_+} \\ & \times (1-\frac{r_2-r_3}{r_2-r_+}\frac{\Pi(h_+|k_r)}{K(k_r)}) - (+\leftrightarrow -)))\,, \end{aligned} \quad (78)$$

and

$$\tilde{\Upsilon}_{t,z} = -a^2\mathcal{E} + \frac{\mathcal{E}\mathcal{Q}}{(1-\mathcal{E}^2)z_1^2}\left(1-\frac{E(k_z)}{K(k_z)}\right)\,. \quad (79)$$

This thus completes the analytic solutions for the r and t coordinates, with the solution for the z coordinate also given. The solution to the ϕ coordinate is not necessary for this project, however, can be found in Van de Meent's paper [12].

Relation to Impact Times

With these equations, the intersections are thus calculated as

$$t_{I,n} = \left[t\left(\frac{n\pi}{\Upsilon_z}\right) - t(0)\right] - t_s\,, \quad n\in\mathbb{Z}\,. \quad (80)$$

where t_s is the time shift parameter, fitted for in the optimisation algorithm.

Integer multiples of the half period $\Lambda_z/2 = \pi/\Upsilon_z$ are calculated and correspond to the impact times of the orbit with the accretion disk. The periodicity of the Mino time solution is exploited here, allowing us to calculated merely a discrete sequence of values rather than the entire orbit. We are also justified in this approach since the convention of the solutions states that $q_z = 0$ corresponds to $z = 0$ meaning that when taking $q_{z,0} = 0$, the value of q_z at $\lambda = 0$ corresponds to when $z = \cos\theta = 0 \Rightarrow \theta = \pi/2$ which is the plane that the accretion disk lies.

References

[1] Lankeswar Dey, Achamveedu Gopakumar, Mauri Valtonen, Stanislaw Zola, Abhimanyu Susobhanan, Rene Hudec, Pauli Pihajoki, Tapio Pursimo, Andrei Berdyugin, Vilppu Piirola, et al. The unique blazar OJ 287 and its massive binary black hole central engine. *Universe*, 5(5):108, 2019.

[2] José L Gómez, Efthalia Traianou, Thomas P Krichbaum, Andrei P Lobanov, Antonio Fuentes, Rocco Lico, Guang-Yao Zhao, Gabriele Bruni, Yuri Y Kovalev, Anne Lähteenmäki, et al. Probing the innermost regions of AGN jets and their magnetic fields with radioastron. V. space and ground millimeter-vlbi imaging of OJ 287. *The Astrophysical Journal*, 924(2):122, 2022.

[3] MJ Valtonen, HJ Lehto, A Sillanpää, K Nilsson, S Mikkola, R Hudec, M Basta, H Teräsranta, S Haque, and H Rampadarath. Predicting the next outbursts of OJ 287 in 2006-2010. *The Astrophysical Journal*, 646(1):36, 2006.

[4] A Sillanpaa, S Haarala, MJ Valtonen, B Sundelius, and GG Byrd. OJ 287-binary pair of supermassive black holes. *The Astrophysical Journal*, 325:628–634, 1988.

[5] JI Katz. A precessing disk in OJ 287? *The Astrophysical Journal*, 478(2):527, 1997.

[6] Seppo Laine, Lankeswar Dey, Mauri Valtonen, A Gopakumar, Stanislaw Zola, S Komossa, Mark Kidger, Pauli Pihajoki, José L Gómez, Daniel Caton, et al. Spitzer observations of the predicted eddington flare from blazar OJ 287. *The Astrophysical Journal Letters*, 894(1):L1, 2020.

[7] Lankeswar Dey, MJ Valtonen, A Gopakumar, S Zola, R Hudec, P Pihajoki, S Ciprini, K Matsumoto, K Sadakane, M Kidger, et al. Authenticating the presence of a relativistic massive black hole binary in OJ 287 using its general relativity centenary flare: Improved orbital parameters. *The Astrophysical Journal*, 866(1):11, 2018.

[8] Eric Poisson and Clifford M Will. Gravity. *Gravity*, 2014.

[9] Steve Drasco and Scott A Hughes. Gravitational wave snapshots of generic extreme mass ratio inspirals. *Physical Review D*, 73(2):024027, 2006.

[10] Wolfram Schmidt. Celestial mechanics in kerr spacetime. *Classical and Quantum Gravity*, 19(10):2743, 2002.

[11] Ryuichi Fujita and Wataru Hikida. Analytical solutions of bound timelike geodesic orbits in kerr spacetime. *Classical and Quantum Gravity*, 26(13):135002, 2009.

[12] Maarten Van de Meent. Analytic solutions for parallel transport along generic bound geodesics in kerr spacetime. *Classical and Quantum Gravity*, 37(14):145007, 2020.

[13] Pauli Pihajoki. Black hole accretion disc impacts. *Monthly Notices of the Royal Astronomical Society*, 457(2):1145–1161, 2016.

[14] Ni I Shakura and Rashid Alievich Sunyaev. Black holes in binary systems. observational appearance. *Astronomy and Astrophysics*, 24:337–355, 1973.

[15] AR King, JE Pringle, RG West, and M Livio. Variability in black hole accretion discs. *Monthly Notices of the Royal Astronomical Society*, 348(1):111–122, 2004.

[16] Nibedita Kalita, Alok C Gupta, and Minfeng Gu. Temporal and spectral variability of OJ 287 before the April–June 2020 outburst. *Galaxies*, 8(3):58, 2020.

[17] Yu E Lyubarskii. Flicker noise in accretion discs. *Monthly Notices of the Royal Astronomical Society*, 292(3):679–685, 1997.

[18] Philip S Cowperthwaite and Christopher S Reynolds. Nonlinear dynamics of accretion disks with stochastic viscosity. *The Astrophysical Journal*, 791(2):126, 2014.

[19] J Drew Hogg and Christopher S Reynolds. Testing the propagating fluctuations model with a long, global accretion disk simulation. *The Astrophysical Journal*, 826(1):40, 2016.

[20] Eric Thrane and Colm Talbot. An introduction to bayesian inference in gravitational-wave astronomy: parameter estimation, model selection, and hierarchical models. *Publications of the Astronomical Society of Australia*, 36, 2019.

[21] Edward Herbst and Frank Schorfheide. Bayesian inference for dsge models. *Manuscript. Board of Governors of the Federal Reserve System, Washington, DC*, 2014.

[22] Scott Kirkpatrick, C Daniel Gelatt Jr, and Mario P Vecchi. Optimization by simulated annealing. *science*, 220(4598):671–680, 1983.

[23] David Luengo, Luca Martino, Mónica Bugallo, Víctor Elvira, and Simo Särkkä. A survey of monte carlo methods for parameter estimation. *EURASIP Journal on Advances in Signal Processing*, 2020(1):1–62, 2020.

[24] Nicholas Metropolis, Arianna W Rosenbluth, Marshall N Rosenbluth, Augusta H Teller, and Edward Teller. Equation of state calculations by fast computing machines. *The journal of chemical physics*, 21(6):1087–1092, 1953.